science.sciencemag.org/content/371/6525/eabd4914/suppl/DC1

Supplementary Materials for

Tubulin glycylation controls axonemal dynein activity, flagellar beat, and male fertility

Sudarshan Gadadhar*, Gonzalo Alvarez Viar†, Jan Niklas Hansen†, An Gong†, Aleksandr Kostarev, Côme Ialy-Radio, Sophie Leboucher, Marjorie Whitfield, Ahmed Ziyyat, Aminata Touré, Luis Alvarez*†, Gaia Pigino*†, Carsten Janke*

†These authors contributed equally to this work.
*Corresponding author. Email: carsten.janke@curie.fr (C.J.); sudarshan.gadadhar@curie.fr (S.G.); pigino@mpi-cbg.de (G.P.); luis.alvarez@caesar.de (L.A.)

Published 8 January 2020, *Science* **371**, eabd4914 (2020)
DOI: 10.1126/science.abd4914

This PDF file includes:

Other Supplementary Material for this manuscript includes the following:
(available at science.sciencemag.org/content/371/6525/eabd4914/suppl/DC1)

MDAR Reproducibility Checklist (.pdf)
Tables S1 and S3 (.xlsx)
Movies S1 to S6 (.mov)

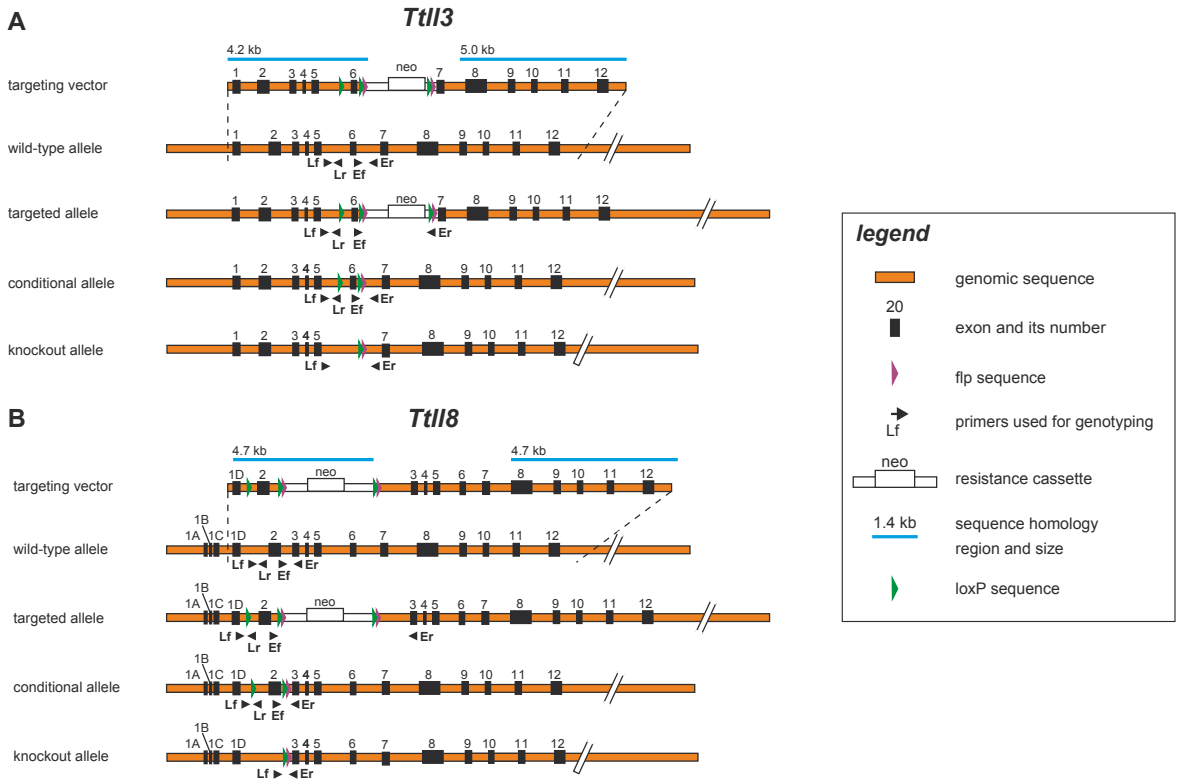

C

mouse strain	primer nr	primer name	primer sequence (5'-3')
Ttll3	P2324	TTLL3_4923-F	CAGGGAGTCCAGGGGAAGCCC
	P1617	TTLL3_41827_R2	GATGGCCCCTGGTCCCTCTACCC
	P1537	CAS_R1_Term	CTTGTTGATATCGTGGTATCGTTATGCGCC
Ttll8	P2029	TTLL8_Ef_7161	GGACAGTACAGTGTTTAGTGTGTGC
	P2030	TTLL8_Er_7164	CCTGCACTGGGTAGTCTTGAAC
	P2033	TTLL8_L3r_7163	CCACTGGAAGATCTGATCCTATCCAG

D

mouse strain	PCR id	PCD product size (bp)	primer mix	annealing		elongation		n° of cycles
				time (s)	temp (°C)	time (s)	temp (°C)	
Ttll3	**PCR1**	550(WT)	P2324 + P1617	30	58	30 + 1/cycle	72	33
	PCR2	250(KO)	P2324 + P1537					
Ttll8	**PCR1**	241(WT)	P2029 + P2030	30	60	60	72	34
	PCR4	1100(WT) / 280(KO)	P2029 + P2033					

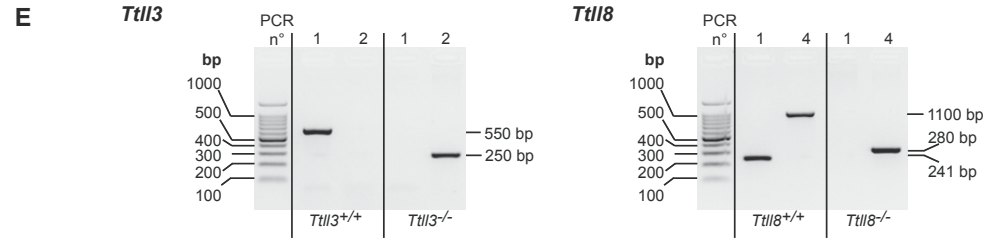

Figure S1: Mouse generation and genotyping

(**A**) Schematic representation (in scale) of the targeting vector used and all possible alleles of the *Ttll3* gene. Orange bar: genomic DNA. Black box: exons with their corresponding number. Green and purple arrowheads: LoxP and Flp sequences, respectively. White bar: *neo* cassette, with the neomycin resistance gene (white box). Blue lines: zone of sequence homology for homologous recombination, with the corresponding sizes. Black arrowheads: primers used for PCR genotyping. **(B)** Schematic representation (in scale) of the targeting vector used and all the possible alleles of the *Ttll8* gene with all the elements the same as that described above. (**C**) List of primers used for genotyping PCRs. (**D**) PCR protocols used for genotyping. (**E**) Representative genotyping results of both *Ttll3* and *Ttll8* transgenes and their knockouts used in this study. PCR products were separated on 2% TBE-agarose gels for 30 min.

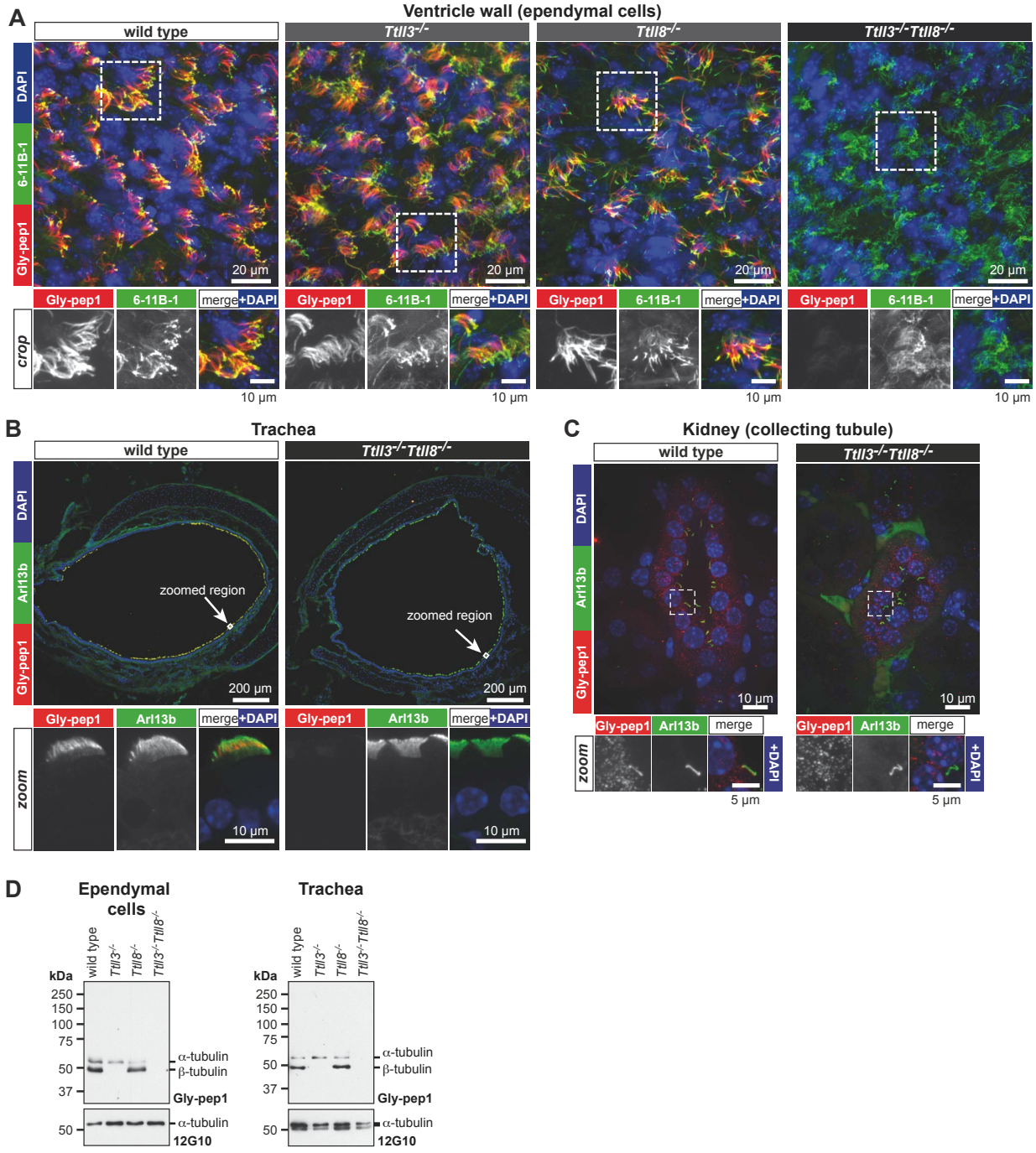

Figure S2: Loss of glycylation in ciliated tissues of *Ttll3*$^{-/-}$*Ttll8*$^{-/-}$ mice

(A) Immunostaining of whole-mount ventricle walls from PN15 wild-type, *Ttll3*$^{-/-}$, *Ttll8*$^{-/-}$, and *Ttll3*$^{-/-}$*Ttll8*$^{-/-}$ ventricles stained for acetylation (6-11B-1, green), glycylation (Gly-pep1, red), and DNA (DAPI, blue). While ependymal cilia in wild-type, *Ttll3*$^{-/-}$ and *Ttll8*$^{-/-}$ mice are positive for glycylation, no glycylation was detected in cilia of *Ttll3*$^{-/-}$*Ttll8*$^{-/-}$ ventricles, while cilia were still present as seen with acetylated tubulin. Scale bar in the crop images: 10 µm. **(B)** Immunostaining of paraffin-embedded sections of trachea for glycylation (Gly-pep1, red) and the cilia membrane (Arl13b; green) show the presence of epithelial cilia in both, wild type and *Ttll3*$^{-/-}$*Ttll8*$^{-/-}$, while glycylation is not detected in *Ttll3*$^{-/-}$*Ttll8*$^{-/-}$ trachea. **(C)** Immunostaining of paraffin-embedded kidney sections for glycylation (Gly-pep1, red) and the cilia membrane (Arl13b; green) show the presence of primary cilia in both, wild-type and *Ttll3*$^{-/-}$*Ttll8*$^{-/-}$ kidney tubules, despite the absence of glycylation in the *Ttll3*$^{-/-}$*Ttll8*$^{-/-}$ cilia. **(D)** Immunoblots of whole-cell lysates of cultured ependymal cells, and from isolated trachea from wild-type, *Ttll3*$^{-/-}$, *Ttll8*$^{-/-}$ and *Ttll3*$^{-/-}$*Ttll8*$^{-/-}$ mice probed with Gly-pep1 for glycylation, and with 12G10 for α-tubulin. As observed for sperm (Fig. 1B), glycylation was partially lost in *Ttll3*$^{-/-}$ and *Ttll8*$^{-/-}$, while the PTM was completely absent in *Ttll3*$^{-/-}$*Ttll8*$^{-/-}$ mice.

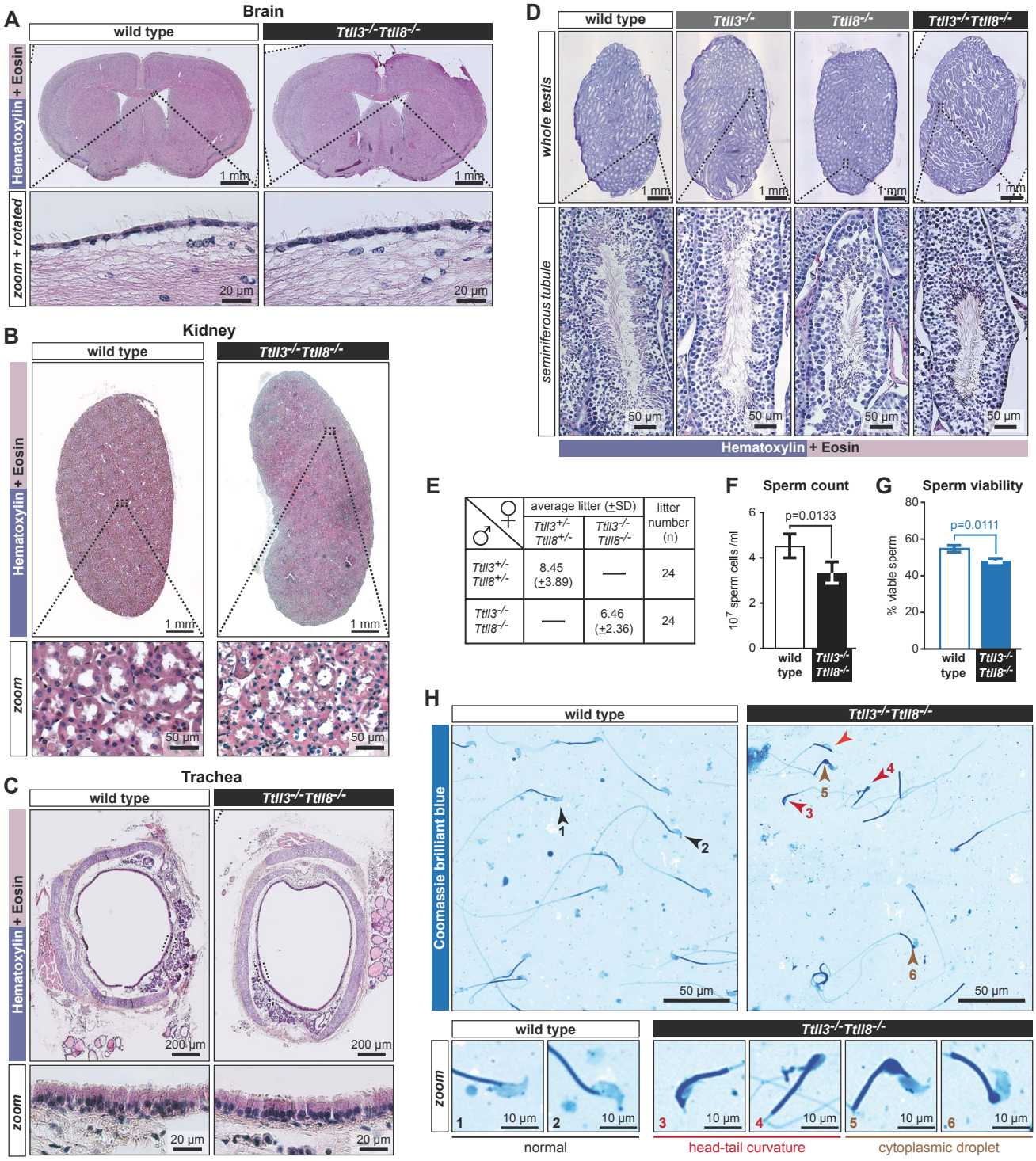

Figure S3: Absence of gross defects in *Ttll3*$^{-/-}$*Ttll8*$^{-/-}$ mice tissues

(A-C) Hematoxylin-Eosin staining of tissues from 6-month-old wild-type and *Ttll3*$^{-/-}$*Ttll8*$^{-/-}$ mice revealed **(A)** no obvious defects in the tissue architecture of the brain. The ventricles of *Ttll3*$^{-/-}$*Ttll8*$^{-/-}$ mice looked normal and showed no signs of hydrocephalus. Closer observation revealed regular arrangement of multiciliated ependymal cells along the wall of the ventricle. The kidney of *Ttll3*$^{-/-}$*Ttll8*$^{-/-}$ mice **(B)** showed no histological defects and absence of any cysts. The kidney tubules appear properly distributed despite the absence of glycylation. The trachea **(C)** appears normal in both, wild-type and *Ttll3*$^{-/-}$*Ttll8*$^{-/-}$ mice with proper arrangement of the columnar multiciliated epithelia. **(D)** Hematoxylin-Eosin stained testes from 6-month-old wild-type, *Ttll3*$^{-/-}$, *Ttll8*$^{-/-}$ and *Ttll3*$^{-/-}$*Ttll8*$^{-/-}$ mice reveal no obvious defects in the tissue architecture of testes. Seminiferous tubules were of the same size, and the arrangement of developing sperm cells within the tubules appeared normal, indicating no defects in the process of spermatogenesis. **(E)** Numerical values of the litter

sizes for the cross between *Ttll3*$^{+/-}$*Ttll8*$^{+/-}$ and *Ttll3*$^{-/-}$*Ttll8*$^{-/-}$ mice (corresponding to Fig. 2A). A total of 24 litters were quantified for each mating scheme. **(F)** Counting of mature spermatozoa obtained from the cauda epididymides of wild-type and *Ttll3*$^{-/-}$*Ttll8*$^{-/-}$ mice revealed no significant alteration in the total sperm count of *Ttll3*$^{-/-}$*Ttll8*$^{-/-}$ mice. **(G)** Sperm viability analysis: Mature sperm isolated from wild-type and *Ttll3*$^{-/-}$*Ttll8*$^{-/-}$ mice were stained with eosine-nigrosin and counted. Sperm viability was slightly reduced in *Ttll3*$^{-/-}$*Ttll8*$^{-/-}$ mice. **(H)** Smears of mature spermatozoa from wild-type and *Ttll3*$^{-/-}$*Ttll8*$^{-/-}$ mice were stained with Coomassie brilliant blue. Note that *Ttll3*$^{-/-}$*Ttll8*$^{-/-}$ spermatozoa show morphological defects such as abnormal curving of the flagellum around the sperm head (red arrowheads, zoom panels 3, 4) and the retention of cytoplasmic droplets (brown arrowheads, zoom panels 5, 6).

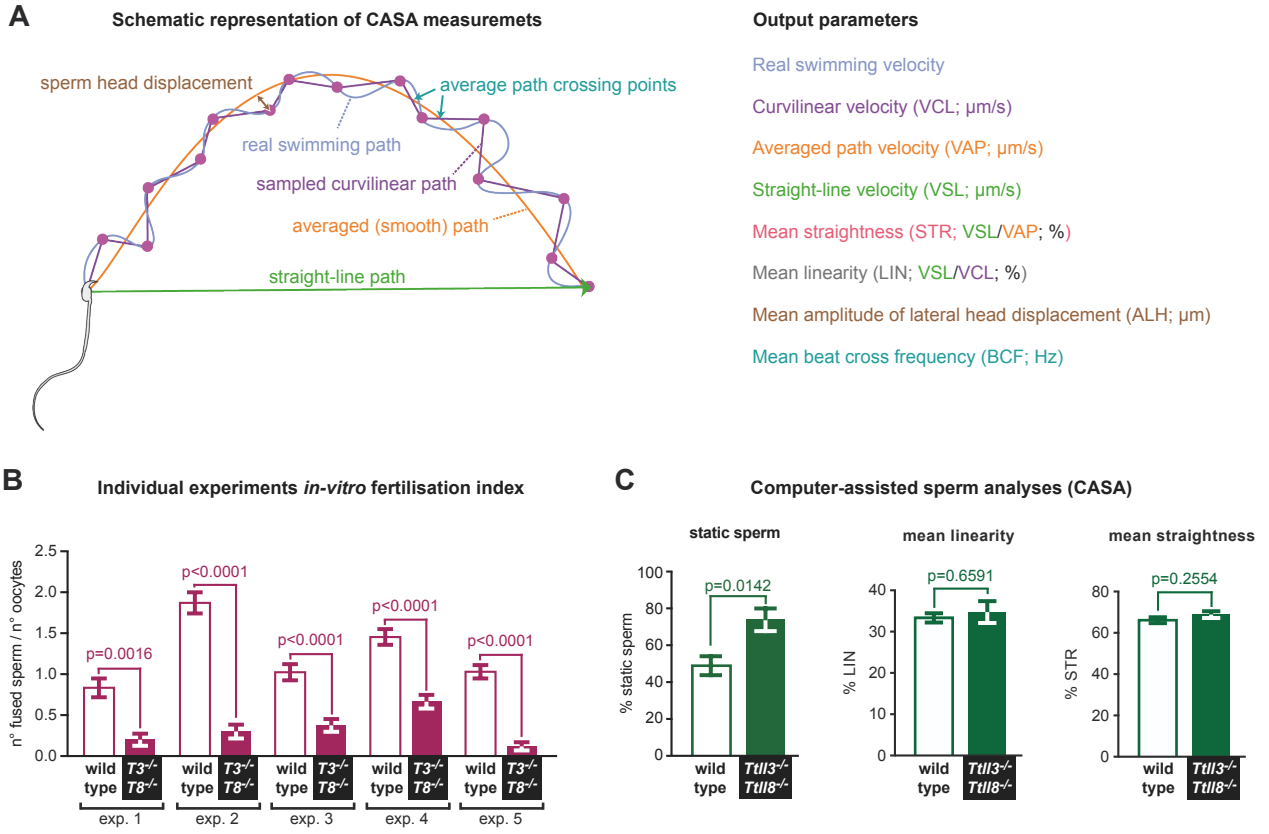

Figure S4: *Ttll3*$^{-/-}$*Ttll8*$^{-/-}$ mice are subfertile with sperm having reduced progressive motility

(A) Schematic representation of sperm motility parameters analyzed by computer-assisted sperm analyses (CASA). The real swimming path (blue) of a single sperm cell is sampled at the acquisition frequency of the recording camera as the curvilinear path (pink). This swimming path is further averaged into a smooth curve (orange) and superimposed onto the wiggling path due to the periodic beating of the cell. The net forward motion of the sperm cell after a specific time interval (typically 1 s in CASA) is the straight-line path (green). The velocities corresponding to these different paths are depicted in the scheme, which include curvilinear velocity (VCL), straight-line velocity (VSL) and average path velocity (VAP). The ratios of these velocities are used to quantify the path linearity (LIN; VSL/VCL) and straightness of the average path (STR; VSL/VAP). CASA also analyses the displacement of the sperm head, determined as the amplitude of lateral head displacement (ALH), and the time-averaged frequency at which the curvilinear path crosses the average path: the beat-cross frequency (BCF). **(B)** *In vitro* fertilization test: Individual experiments of the *in vitro* fertilization analysis performed with wild-type and *Ttll3*$^{-/-}$*Ttll8*$^{-/-}$ mice. An average of all the experiments depicted here is shown in Fig. 2B. **(C)** Analysis of the motility of wild-type and *Ttll3*$^{-/-}$*Ttll8*$^{-/-}$ sperm by CASA: Various parameters of sperm motility were analyzed for both wild-type and *Ttll3*$^{-/-}$*Ttll8*$^{-/-}$ mice. *Ttll3*$^{-/-}$*Ttll8*$^{-/-}$ mice showed a clear increase in the proportion of static sperm in comparison to wild-type sperm while there was no change in the mean linearity and straightness.

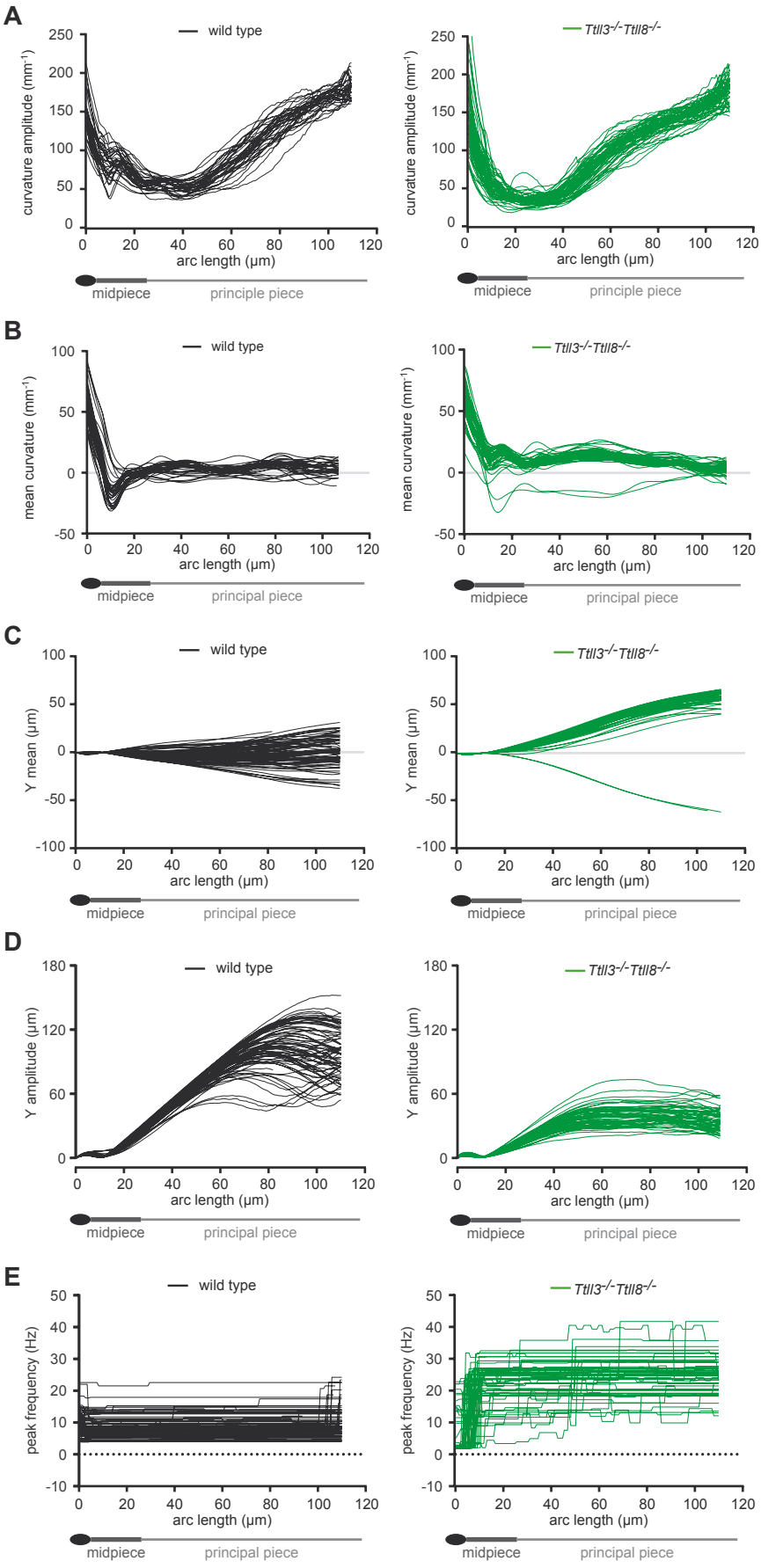
A
wild type
Ttll3-/-Ttll8-/-
curvature amplitude (mm-1)
arc length (µm)
midpiece
principle piece
B
wild type
Ttll3-/-Ttll8-/-
mean curvature (mm-1)
arc length (µm)
midpiece
principal piece
C
wild type
Ttll3-/-Ttll8-/-
Y mean (µm)
arc length (µm)
midpiece
principal piece
D
wild type
Ttll3-/-Ttll8-/-
Y amplitude (µm)
arc length (µm)
midpiece
principal piece
E
wild type
Ttll3-/-Ttll8-/-
peak frequency (Hz)
arc length (µm)
midpiece
principal piece

Figure S5: Extended data for 2D analyses of the flagellar beat

(A) Individual traces from both, wild-type and *Ttll3*$^{-/-}$*Ttll8*$^{-/-}$ sperm, showing the flagellar curvature range. **(B)** Individual traces from wild-type and *Ttll3*$^{-/-}$*Ttll8*$^{-/-}$ sperm used to calculate the mean (±SD) for the analyses of mean flagellar curvature (Fig. 3B). **(C)** Individual traces from wild-type and *Ttll3*$^{-/-}$*Ttll8*$^{-/-}$ sperm for the time-averaged flagellar position in the direction perpendicular to the head-midpiece-axis (Y average). **(D)** Individual traces from wild-type and *Ttll3*$^{-/-}$ *Ttll8*$^{-/-}$ sperm used to calculate the mean (±SD) for the analyses of the flagellar amplitude in the direction perpendicular to the head-midpiece-axis (Y amplitude; Fig. 3C). **(E)** Individual traces from wild-type and *Ttll3*$^{-/-}$*Ttll8*$^{-/-}$ sperm used to calculate the mean (±SD) for flagellar peak frequency (Fig. 3D).

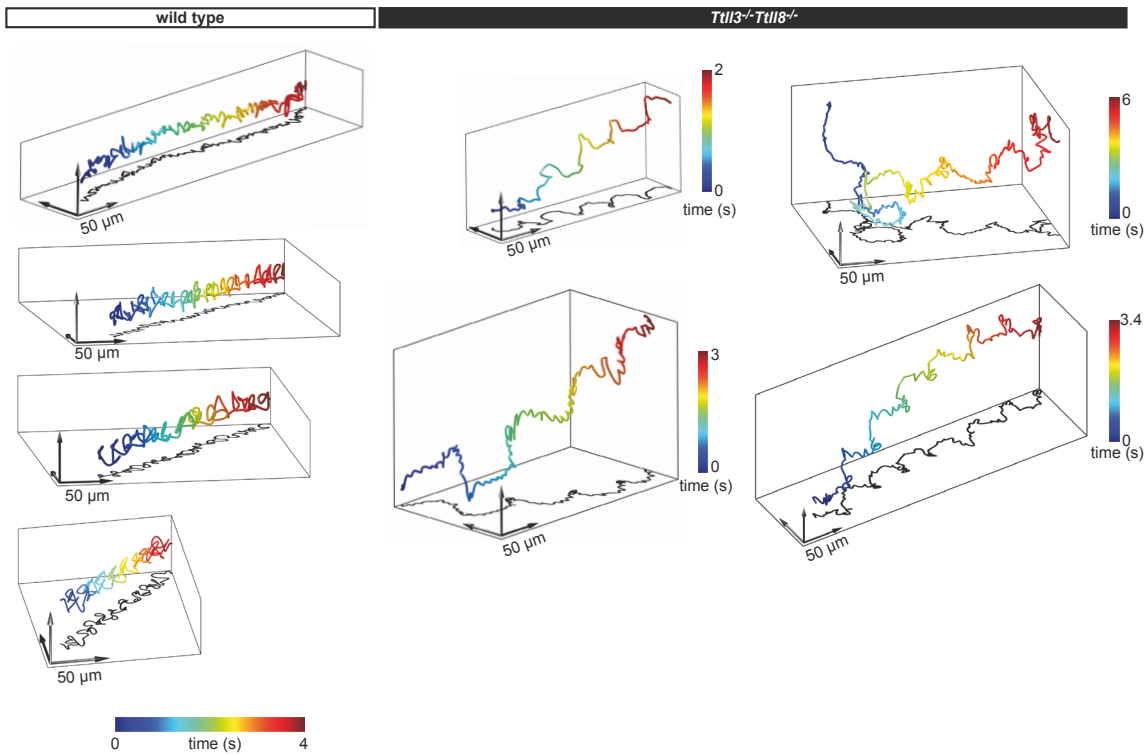

Figure S6: Extended data for 3D motility analyses

Gallery of 3D swimming paths of individual wild-type and *Ttll3*$^{-/-}$*Ttll8*$^{-/-}$ sperm recorded using high-speed in-line holography. Time is color-coded.

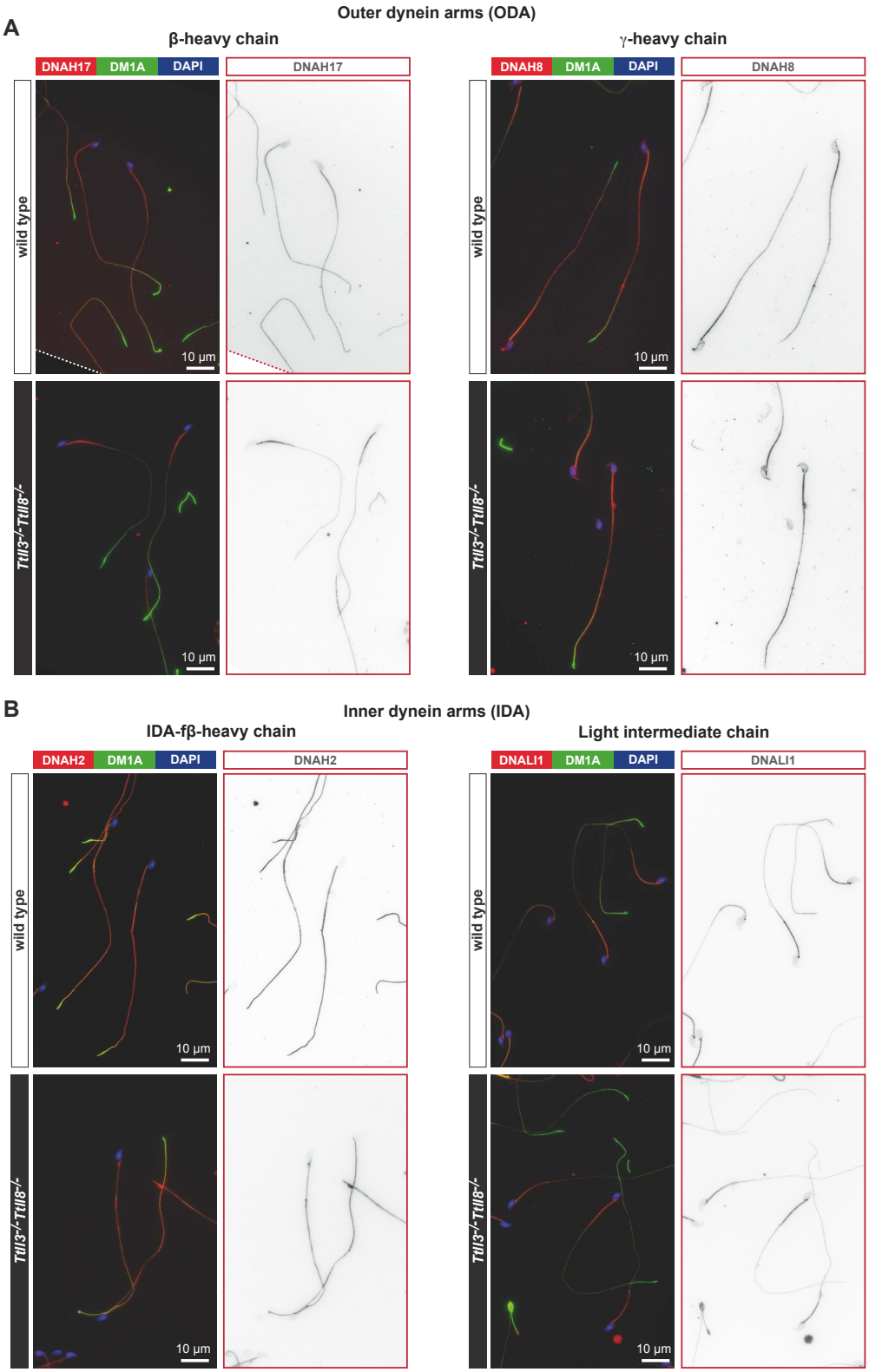

Figure S7: Distribution of axonemal dynein isoforms along flagella is not affected in *Ttll3*$^{-/-}$*Ttll8*$^{-/-}$ sperm

Immunostaining of wild-type and *Ttll3*$^{-/-}$*Ttll8*$^{-/-}$ sperm smears for **(A)** ODAs: DNAH17 (β-heavy chain; red) and DNAH8 (γ-heavy chain; red), and **(B)** IDAs: DNAH2 (IDA-fβ; red) and DNALI1 (light intermediate chain; red). MTs are visualized by α-tubulin staining (DM1A; green), and DNA with DAPI (blue). Nuclear staining shows normal sperm head morphology. The negative greyscale images for DNAH8 and DNAH17 (A), as well as for DNAH2 and DNALI1 and show that the distribution of ODAs and IDAs is identical in flagella of wild-type and *Ttll3*$^{-/-}$*Ttll8*$^{-/-}$ sperm.

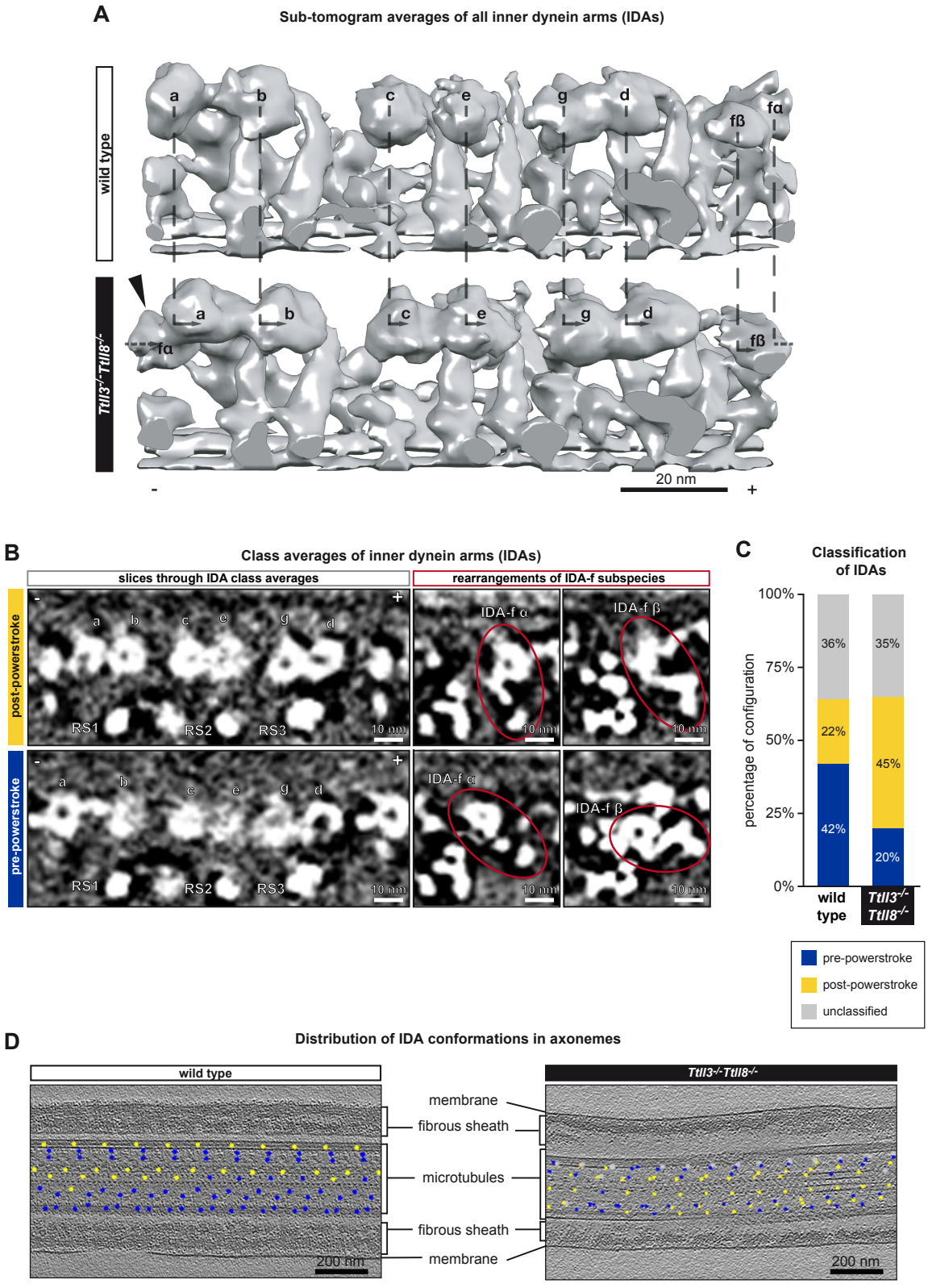

Figure S8: Inner dynein arms (IDAs) are affected in *Ttll3*$^{-/-}$*Ttll8*$^{-/-}$ sperm

(A) Subtomogram average of IDAs from wild-type (top) and *Ttll3*$^{-/-}$*Ttll8*$^{-/-}$ (bottom) sperm axonemes. The average from the *Ttll3*$^{-/-}$*Ttll8*$^{-/-}$ sperm indicate that all IDA heavy chains are shifted towards the MT plus-end (+) as compared to wild type. For clarity, the different IDAs are only marked by their subtype-classifying letter (a: IDA-a etc.). The largest shift is observed for IDA-fα. Similar shifts are known from the post-powerstroke conformation of IDAs in sea urchin sperm

(*34*). Dashed lines: approximate position of the AAA domain center of IDAs in wild-type axonemes; arrows: shift of the AAA domains between wild-type and *Ttll3*$^{-/-}$*Ttll8*$^{-/-}$ axonemes. **(B)** Slices through class averages generated from IDA classification showing their overall transition between pre-powerstroke and post-powerstroke conformations (left). Particularly consistent rearrangements of IDA-f subspecies (encircled in red) between the two classes are shown in the right panels. **(C)** Incidence of the distinct IDA conformations in wild-type (n=960) and *Ttll3*$^{-/-}$*Ttll8*$^{-/-}$ (n=600) axonemes. Unclassifiable subtomograms were excluded. *Ttll3*$^{-/-}$*Ttll8*$^{-/-}$ flagella have particularly increased percentage of post-powerstroke conformations. **(D)** Distribution of the different IDA conformations visualized in wild-type and *Ttll3*$^{-/-}$*Ttll8*$^{-/-}$ axonemes shows clear reduction of pre-powerstroke conformations, coupled to increased post-powerstroke conformations in *Ttll3*$^{-/-}$*Ttll8*$^{-/-}$ sperm (color coding of dots as in C).

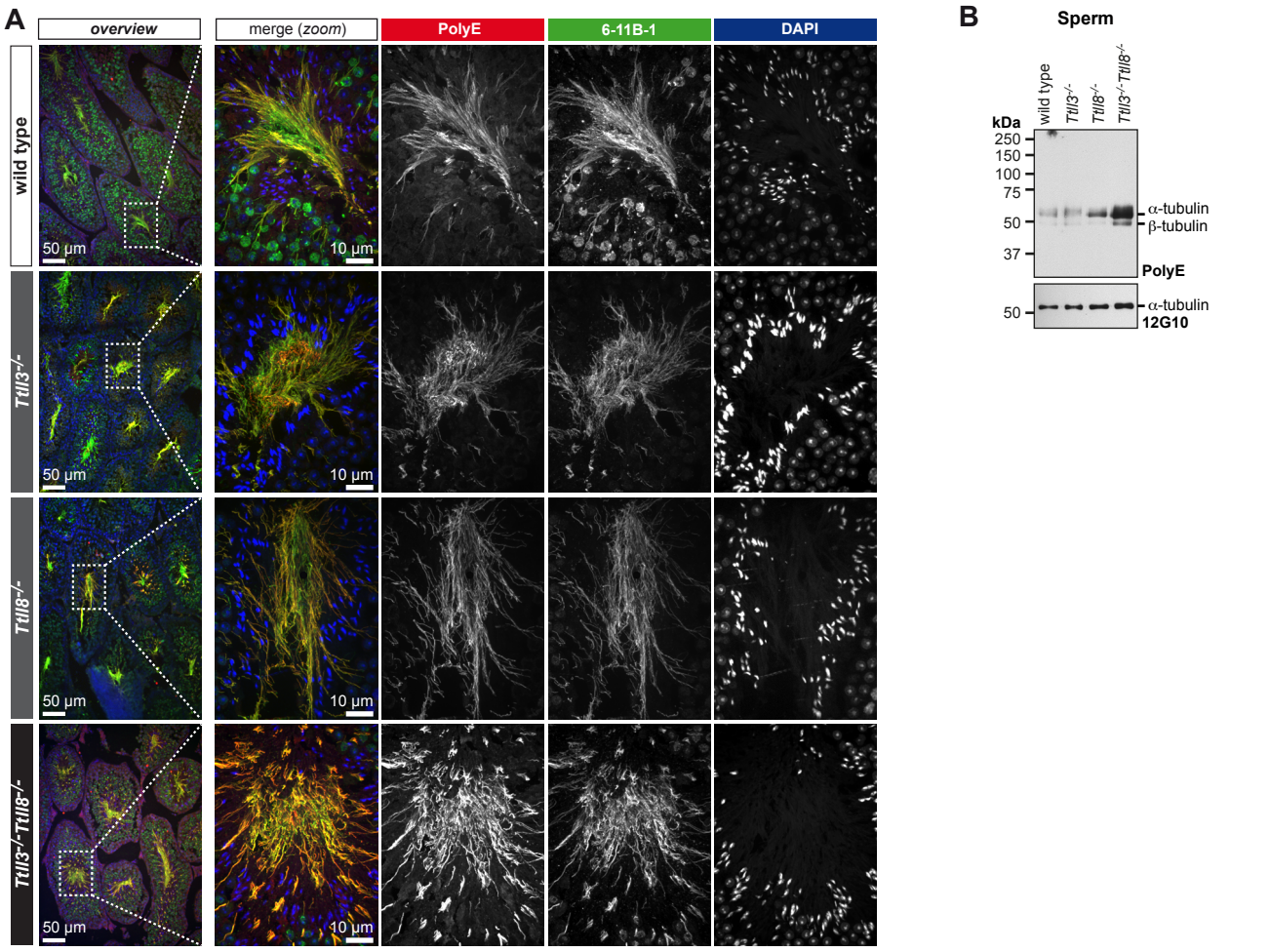

Figure S9: Loss of glycylation leads to increased glutamylation in *Ttll3*$^{-/-}$*Ttll8*$^{-/-}$ sperm

(A) Paraffin-embedded testes sections stained for tubulin acetylation (6-11B-1; green), glutamylation (PolyE; red), and DNA (DAPI). Nuclear staining shows normal sperm head morphology and a normal arrangement of sperm heads of different developmental stages in the seminiferous tubules of wild-type, *Ttll3*$^{-/-}$, *Ttll8*$^{-/-}$ and *Ttll3*$^{-/-}$*Ttll8*$^{-/-}$ testes. Flagella from *Ttll3*$^{-/-}$*Ttll8*$^{-/-}$ sperm show increased polyglutamylation compared to the wild-type and the single knockout sperm. **(B)** Immunoblot of sperm samples from wild-type, *Ttll3*$^{-/-}$, *Ttll8*$^{-/-}$ and *Ttll3*$^{-/-}$*Ttll8*$^{-/-}$ mice. Note that compared to the wild-type and the single knockout mice (*Ttll3*$^{-/-}$, *Ttll8*$^{-/-}$), there is a substantial increase in polyglutamylation (PolyE) of α-tubulin and a mild increase in β-tubulin in the *Ttll3*$^{-/-}$*Ttll8*$^{-/-}$ sperm. The anti-α-tubulin antibody 12G10 confirmed equal tubulin load.

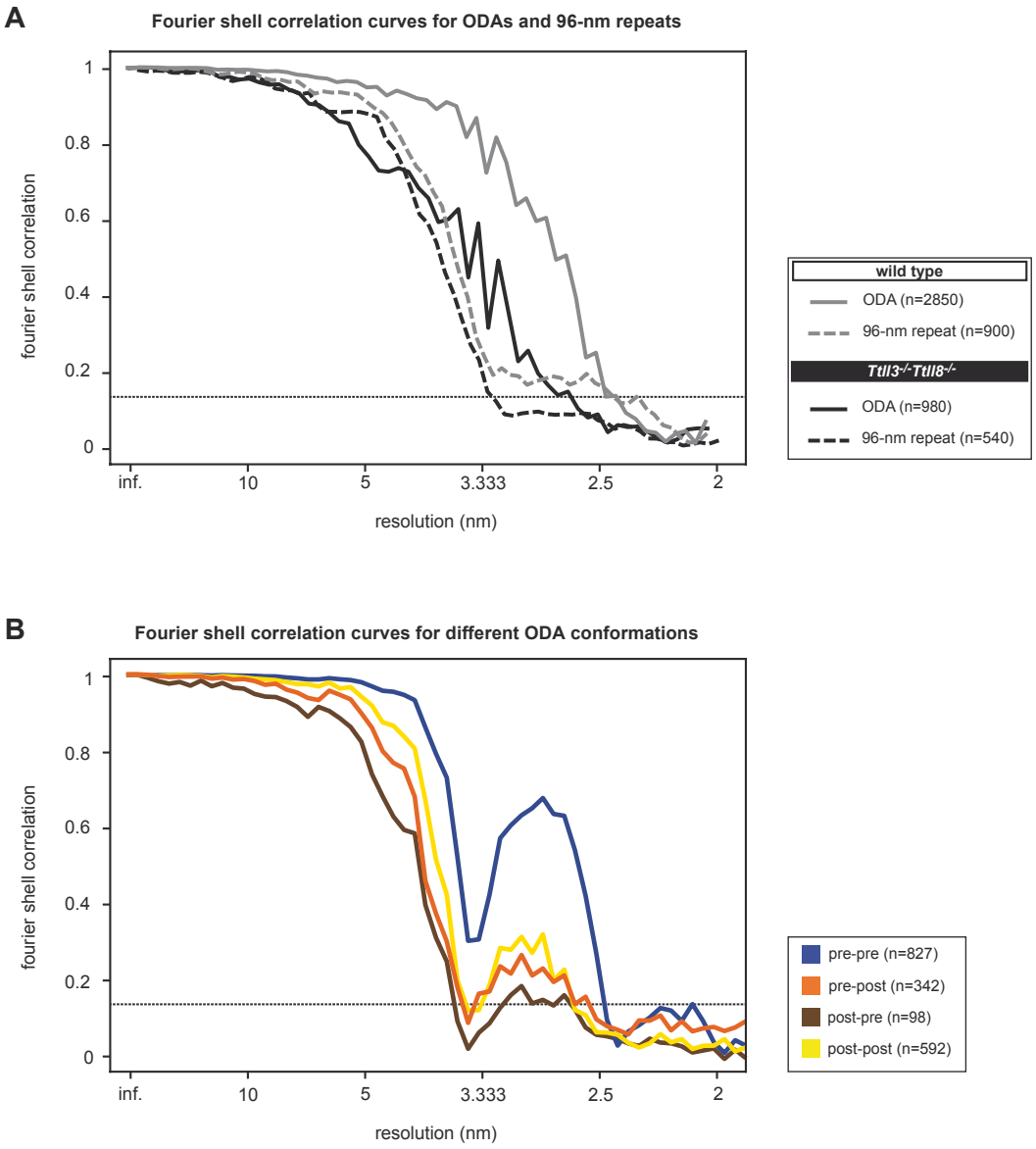

Figure S10: Resolution estimation of ODAs and 96-nm repeat subtomogram averaging maps

(A) Fourier Shell Correlation (FSC) curves from 96-nm repeat and ODA averages provides an estimation of the reliability of the alignment performed on the different datasets and an estimation of their resolution at the typical 0.143 cut-off (indicated by the horizontal dashed line). The inverse of the spatial frequency at which the FSC first crosses the cut-off defines the resolution. The higher the spatial frequency, the better the structural resolution. The inverse of the spatial frequency is here expressed in nm. **(B)** FSC curves from class averages generated from filtered wild-type and *Ttll3*$^{-/-}$*Ttll8*$^{-/-}$ particles. The reduction in particle number due to the splitting of the dataset into classes still does not hinder dynein heavy-chain resolvability.

Table S2: Antibodies used for immunoblotting and immunocytochemistry

Primary Antibody	Reference n°	Antigen	Dilution (Western blot)	Dilution (Immuno-cytochemistry)
Gly-pep1	AdipoGen AG-25B-0034	Branch point glycylation on β-tubulin C-terminal tail, rabbit polyclonal	1:10,000	1:15,000
6-11B-1	Sigma Aldrich T7451	acetylated α-tubulin from the outer arm of sea urchin, mouse monoclonal.	----------	1 :1000
PolyE	Adipogen AG-25B-0030	linear chains of 4 and more glutamate residues, rabbit polyclonal	1:10,000	1:10,000
12G10	Developed by J. Frankel and M. Nelson, obtained from the Developmental Studies Hybridoma Bank, developed under the auspices of the NICHD, and maintained by the University of Iowa.	α-tubulin, mouse monoclonal	1:500	----------
Arl13b	NeuroMab 75-287	Fusion protein amino acids 208-427 (C-terminus) of mouse Arl13b, mouse monoclonal	---------	1:1,000
DNAH8	Sigma Aldrich HPA028447	Recombinant axonemal dynein heavy chain 8 epitope with signature tag (PrEST), rabbit polyclonal	---------	1:500
DNAH17	Sigma Aldrich HPA024354	Recombinant axonemal dynein heavy chain 17 epitope with signature tag (PrEST), rabbit polyclonal	---------	1:200
DNAH2	Sigma Aldrich HPA067103	Axonemal dynein heavy chain 2, rabbit polyclonal	---------	1:100
DNALI1	Sigma Aldrich HPA028305	Recombinant axonemal dynein light intermediate chain 1 epitope with signature tag (PrEST), rabbit polyclonal	---------	1:50
DM1A	Sigma Aldrich T9026	α-tubulin, mouse monoclonal	---------	1:500

Secondary Antibody	**Reference n°**	**Antigen**	**Dilution (Western blot)**	**Dilution (Immuno-cytochemistry)**
Goat-anti rabbit IgG-HRP	Bethyl Laboratories Inc. A120-201P	Rabbit whole IgG	1:10,000	---------
Goat-anti mouse IgG-HRP	Bethyl Laboratories Inc. A90-516P	Mouse whole IgG	1:10,000	----------
Goat-anti mouse IgG Alexa Fluor 488	Thermo Fisher Scientific. A11001	Mouse Gamma immunoglobins heavy and light chains	---------	1 :1,000
Goat-anti mouse IgG2a Alexa Fluor 488	Thermo Fisher Scientific. A21131	Mouse IgG 2a	---------	1 :1,000
Goat-anti rabbit IgG Alexa Fluor 568	Thermo Fisher Scientific. A11036	Rabbit Gamma immunoglobins heavy and light chains	---------	1 :1,000

Legends to Tables

Table S1: Quantification of sperm quality, swim pattern and *in vitro* fertilization index: Tables showing the data from individual experiments for the different motility parameters determined by CASA (Fig. 2C, fig. S4C), the sperm count (fig. S3F), sperm viability (fig. S3G), swimming behaviour (Fig. 4F), and the *in vitro* fertilization index (Fig. 2B, fig. S4B).

Table S3: Quantifications from analysis using SpermQ software: Tables corresponding to the SpermQ analysis of mean curvature (Fig. 3B, fig. S5A and S5B), flagellar amplitude (Fig. 3C, fig. S5D) and peak frequency (Fig. 3D, fig. S5E) of individual sperm cells from different wild-type and *Ttll3*$^{-/-}$*Ttll8*$^{-/-}$ mice.

Legends to Movies

Movie S1: Flagellar beat of sperm tethered at their heads

Dark-field microscopy of head-tethered sperm recorded at 250 frames-per-second (fps). **(A)** Symmetric and asymmetric flagellar beat for wild-type and *Ttll3*$^{-/-}$*Ttll8*$^{-/-}$ sperm, respectively (top). The symmetry of the beat is clearly shown in the corresponding color-coded flagellar beat projections (bottom panels from Fig. 3A). **(B** to **D)** Flagellar beat analyses of tethered sperm (panels from Fig. 3, B to D): *Ttll3*$^{-/-}$*Ttll8*$^{-/-}$ sperm have a more than three times higher curvature **(B)** and less than half the beat amplitude **(C)**. The beat frequency **(D)** is asymmetric: it is lower near the sperm head, but more than double in the rest of the flagellum.

Movie S2: Swimming behaviors of sperm

Dark-field microscopy of free-swimming sperm from wide-field images **(A** and **B)** were recorded at 50 fps. Single-sperm transitions **(C** to **E)** were recorded at 250 fps. Wild-type sperm swim almost exclusively along an elongated curvilinear path **(A** and **C)**. In contrast, most *Ttll3*$^{-/-}$*Ttll8*$^{-/-}$ sperm (~86%) swim in circular paths **(B** and **E)**, with a small fraction (~14%) showing incidental progressive motility **(B** and **D)**.

Movie S3: Helical and circular swimming of *Ttll3*$^{-/-}$*Ttll8*$^{-/-}$ sperm

Dark-field microscopy of free-swimming sperm recorded at 250 fps in custom-made observation chambers of 100 μm depth. Upon reaching the wall of the observation chamber, the *Ttll3*$^{-/-}$*Ttll8*$^{-/-}$ sperm transitions from helical to circular swimming (still panel from Fig. 4D).

Movie S4: Absence of glycylation results in altered conformations of axonemal ODA heavy chains

(A) Fitting the crystal structures of the dynein motor domain onto isosurface renderings of the 96-nm repeats in sperm axoneme shows an altered conformation of both β-heavy chain (magenta) and γ-heavy chain (green) when the dynein shifts from pre-powerstroke to the post-powerstroke condition. **(B)** Predominant conformations of the ODAs observed in the wild-type and *Ttll3*$^{-/-}$*Ttll8*$^{-/-}$ sperm (panels from Fig. 6A). **(C)** Comparison of the transition of the ODAs shows a coordinated transition from pre-powerstroke (blue) to post-powerstroke (yellow) in the wild-type axonemes, whereas in the *Ttll3*$^{-/-}$*Ttll8*$^{-/-}$ axonemes intermediate conformations, pre-post (orange) and post-pre (brown) are more commonly found (bottom panels from Fig. 6B).

Movie S5: IDA-f conformational reconfiguration is linked to the tilting motion of the nexin-dynein regulatory complex (N-DRC)

(A) Slices through class averages generated from IDA classification showing their overall transition between pre-powerstroke and post-powerstroke conformations (left). Particularly consistent rearrangement of IDA-f subspecies (encircled in red) between the two classes are shown in the right panels (from fig. S8B). **(B)** The conformational reconfiguration of IDA-f occurred synchronously with an opposing tilting motion of the nexin-dynein regulatory complex and the radial-spoke heads. This tilting motion was perpendicular to the MT axis and associated with a displacement of the next MT doublet. (A tub: A-tubule; B tub: B-tubule; N-DRC: nexin-dynein regulatory complex; RS: radial spoke; ODA: outer dynein arm; IDA: inner dynein arm)

Movie S6: Absence of glycylation has no apparent effect on the beating of ependymal cilia

(A) Representative video recordings of ependymal cilia acquired from 100-200-µm sagittal sections of wild-type and *Ttll3*$^{-/-}$*Ttll8*$^{-/-}$ brain ventricles. Recordings were performed at 100 fps for 3 s using a 60× objective. The videos were slowed down 20× to scrutinize the ciliary beat waveform (one representative video in original speed is shown on the left). Visual inspection does not reveal any changes in the beat patterns of multicilia in the absence of glycylation. **(B)** Scatter plots showing the analysis of cilia beat frequencies from three independent experiments with each point representing an individual cell recorded from the same brain slice (number of cells are given). Median (±SEM) is indicated, p-values are determined by Student's t-test. All three experiments coherently show no differences between wild-type and *Ttll3*$^{-/-}$*Ttll8*$^{-/-}$ cells. Note that overall values vary between different experimental days, most likely due to slight variations in imaging conditions (e.g. temperature).

References and Notes

1. C. Janke, M. M. Magiera, The tubulin code and its role in controlling microtubule properties and functions. *Nat. Rev. Mol. Cell Biol.* **21**, 307–326 (2020). doi:10.1038/s41580-020-0214-3 Medline

2. M. H. Bré, V. Redeker, M. Quibell, J. Darmanaden-Delorme, C. Bressac, J. Cosson, P. Huitorel, J. M. Schmitter, J. Rossler, T. Johnson, A. Adoutte, N. Levilliers, Axonemal tubulin polyglycylation probed with two monoclonal antibodies: Widespread evolutionary distribution, appearance during spermatozoan maturation and possible function in motility. *J. Cell Sci.* **109**, 727–738 (1996). Medline

3. K. Rogowski, F. Juge, J. van Dijk, D. Wloga, J.-M. Strub, N. Levilliers, D. Thomas, M.-H. Bré, A. Van Dorsselaer, J. Gaertig, C. Janke, Evolutionary divergence of enzymatic mechanisms for posttranslational polyglycylation. *Cell* **137**, 1076–1087 (2009). doi:10.1016/j.cell.2009.05.020 Medline

4. M. Bosch Grau, G. Gonzalez Curto, C. Rocha, M. M. Magiera, P. Marques Sousa, T. Giordano, N. Spassky, C. Janke, Tubulin glycylases and glutamylases have distinct functions in stabilization and motility of ependymal cilia. *J. Cell Biol.* **202**, 441–451 (2013). doi:10.1083/jcb.201305041 Medline

5. M. Bosch Grau, C. Masson, S. Gadadhar, C. Rocha, O. Tort, P. Marques Sousa, S. Vacher, I. Bieche, C. Janke, Alterations in the balance of tubulin glycylation and glutamylation in photoreceptors leads to retinal degeneration. *J. Cell Sci.* **130**, 938–949 (2017). doi:10.1242/jcs.199091 Medline

6. C. Rocha, L. Papon, W. Cacheux, P. Marques Sousa, V. Lascano, O. Tort, T. Giordano, S. Vacher, B. Lemmers, P. Mariani, D. Meseure, J. P. Medema, I. Bièche, M. Hahne, C. Janke, Tubulin glycylases are required for primary cilia, control of cell proliferation and tumor development in colon. *EMBO J.* **33**, 2247–2260 (2014). doi:10.15252/embj.201488466 Medline

7. S. Gadadhar, H. Dadi, S. Bodakuntla, A. Schnitzler, I. Bièche, F. Rusconi, C. Janke, Tubulin glycylation controls primary cilia length. *J. Cell Biol.* **216**, 2701–2713 (2017). doi:10.1083/jcb.201612050 Medline

8. A. Konno, K. Ikegami, Y. Konishi, H.-J. Yang, M. Abe, M. Yamazaki, K. Sakimura, I. Yao, K. Shiba, K. Inaba, M. Setou, *Ttll9*$^{-/-}$ mice sperm flagella show shortening of doublet 7, reduction of doublet 5 polyglutamylation and a stall in beating. *J. Cell Sci.* **129**, 2757–2766 (2016). doi:10.1242/jcs.185983 Medline

9. R. J. Mullen, E. M. Eicher, R. L. Sidman, Purkinje cell degeneration, a new neurological mutation in the mouse. *Proc. Natl. Acad. Sci. U.S.A.* **73**, 208–212 (1976). doi:10.1073/pnas.73.1.208 Medline

10. P. Vogel, G. Hansen, G. Fontenot, R. Read, Tubulin tyrosine ligase-like 1 deficiency results in chronic rhinosinusitis and abnormal development of spermatid flagella in mice. *Vet. Pathol.* **47**, 703–712 (2010). doi:10.1177/0300985810363485 Medline

11. H.-Y. Wu, P. Wei, J. I. Morgan, Role of cytosolic carboxypeptidase 5 in neuronal survival and spermatogenesis. *Sci. Rep.* **7**, 41428 (2017). doi:10.1038/srep41428 Medline

12. C. Mencarelli, P. Lupetti, R. Dallai, New insights into the cell biology of insect axonemes. *Int. Rev. Cell Mol. Biol.* **268**, 95–145 (2008). doi:10.1016/S1937-6448(08)00804-6 Medline

13. J. F. Reiter, M. R. Leroux, Genes and molecular pathways underpinning ciliopathies. *Nat. Rev. Mol. Cell Biol.* **18**, 533–547 (2017). doi:10.1038/nrm.2017.60 Medline

14. M. A. El-Brolosy, D. Y. R. Stainier, Genetic compensation: A phenomenon in search of mechanisms. *PLOS Genet.* **13**, e1006780 (2017). doi:10.1371/journal.pgen.1006780 Medline

15. M. A. El-Brolosy, Z. Kontarakis, A. Rossi, C. Kuenne, S. Günther, N. Fukuda, K. Kikhi, G. L. M. Boezio, C. M. Takacs, S.-L. Lai, R. Fukuda, C. Gerri, A. J. Giraldez, D. Y. R. Stainier, Genetic compensation triggered by mutant mRNA degradation. *Nature* **568**, 193–197 (2019). doi:10.1038/s41586-019-1064-z Medline

16. R. Talevi, R. Gualtieri, In vivo versus in vitro fertilization. *Eur. J. Obstet. Gynecol. Reprod. Biol.* **115** (suppl. 1), S68–S71 (2004). doi:10.1016/j.ejogrb.2004.01.015 Medline

17. H. H. Pusch, The importance of sperm motility for the fertilization of human oocytes in vivo and in vitro. *Andrologia* **19**, 514–527 (1987). doi:10.1111/j.1439-0272.1987.tb01891.x Medline

18. R. P. Amann, D. Waberski, Computer-assisted sperm analysis (CASA): Capabilities and potential developments. *Theriogenology* **81**, 5–17.e1, 3 (2014). doi:10.1016/j.theriogenology.2013.09.004 Medline

19. Z. Heidary, K. Saliminejad, M. Zaki-Dizaji, H. R. Khorram Khorshid, Genetic aspects of idiopathic asthenozoospermia as a cause of male infertility. *Hum. Fertil.* **23**, 83–92 (2020). doi:10.1080/14647273.2018.1504325 Medline

20. J. N. Hansen, S. Rassmann, J. F. Jikeli, D. Wachten, *SpermQ*—A simple analysis software to comprehensively study flagellar beating and sperm steering. *Cells* **8**, 10 (2018). doi:10.3390/cells8010010 Medline

21. S. T. Mortimer, D. Mortimer, Kinematics of human spermatozoa incubated under capacitating conditions. *J. Androl.* **11**, 195–203 (1990). Medline

22. J. M. Neill, P. Olds-Clarke, A computer-assisted assay for mouse sperm hyperactivation demonstrates that bicarbonate but not bovine serum albumin is required. *Gamete Res.* **18**, 121–140 (1987). doi:10.1002/mrd.1120180204 Medline

23. B. Marquez, G. Ignotz, S. S. Suarez, Contributions of extracellular and intracellular Ca^{2+} to regulation of sperm motility: Release of intracellular stores can hyperactivate CatSper1 and CatSper2 null sperm. *Dev. Biol.* **303**, 214–221 (2007). doi:10.1016/j.ydbio.2006.11.007 Medline

24. T.-W. Su, I. Choi, J. Feng, K. Huang, E. McLeod, A. Ozcan, Sperm trajectories form chiral ribbons. *Sci. Rep.* **3**, 1664 (2013). doi:10.1038/srep01664 Medline

25. J. F. Jikeli, L. Alvarez, B. M. Friedrich, L. G. Wilson, R. Pascal, R. Colin, M. Pichlo, A. Rennhack, C. Brenker, U. B. Kaupp, Sperm navigation along helical paths in 3D chemoattractant landscapes. *Nat. Commun.* **6**, 7985 (2015). doi:10.1038/ncomms8985 Medline

26. R. L. Miller, “Sperm chemo-orientation in the metazoa” in *Biology of Fertilization, Volume 2*, C. B. Metz, A. Monroy, Eds. (Academic Press, 1985), pp. 275–337.

27. T.-W. Su, L. Xue, A. Ozcan, High-throughput lensfree 3D tracking of human sperms reveals rare statistics of helical trajectories. *Proc. Natl. Acad. Sci. U.S.A.* **109**, 16018–16022 (2012). doi:10.1073/pnas.1212506109 Medline

28. J. Elgeti, U. B. Kaupp, G. Gompper, Hydrodynamics of sperm cells near surfaces. *Biophys. J.* **99**, 1018–1026 (2010). doi:10.1016/j.bpj.2010.05.015 Medline

29. A. Gong, S. Rode, U. B. Kaupp, G. Gompper, J. Elgeti, B. M. Friedrich, L. Alvarez, The steering gaits of sperm. *Philos. Trans. R. Soc. London Ser. B* **375**, 20190149 (2020). doi:10.1098/rstb.2019.0149 Medline

30. H. C. Crenshaw, A new look at locomotion in microorganisms: Rotating and translating. *Am. Zool.* **36**, 608–618 (1996). doi:10.1093/icb/36.6.608

31. D. Nicastro, C. Schwartz, J. Pierson, R. Gaudette, M. E. Porter, J. R. McIntosh, The molecular architecture of axonemes revealed by cryoelectron tomography. *Science* **313**, 944–948 (2006). doi:10.1126/science.1128618 Medline

32. R. Viswanadha, W. S. Sale, M. E. Porter, Ciliary motility: Regulation of axonemal dynein motors. *Cold Spring Harbor Perspect. Biol.* **9**, a018325 (2017). doi:10.1101/cshperspect.a018325 Medline

33. M. E. Porter, W. S. Sale, The 9 + 2 axoneme anchors multiple inner arm dyneins and a network of kinases and phosphatases that control motility. *J. Cell Biol.* **151**, F37–F42 (2000). doi:10.1083/jcb.151.5.F37 Medline

34. J. Lin, D. Nicastro, Asymmetric distribution and spatial switching of dynein activity generates ciliary motility. *Science* **360**, eaar1968 (2018). doi:10.1126/science.aar1968 Medline

35. L. Gui, K. Song, D. Tritschler, R. Bower, S. Yan, A. Dai, K. Augspurger, J. Sakizadeh, M. Grzemska, T. Ni, M. E. Porter, D. Nicastro, Scaffold subunits support associated subunit assembly in the *Chlamydomonas* ciliary nexin-dynein regulatory complex. *Proc. Natl. Acad. Sci. U.S.A.* **116**, 23152–23162 (2019). doi:10.1073/pnas.1910960116 Medline

36. J. D. Alper, M. Tovar, J. Howard, Displacement-weighted velocity analysis of gliding assays reveals that *Chlamydomonas* axonemal dynein preferentially moves conspecific microtubules. *Biophys. J.* **104**, 1989–1998 (2013). doi:10.1016/j.bpj.2013.03.041 Medline

37. R. J. McKenney, W. Huynh, R. D. Vale, M. Sirajuddin, Tyrosination of α-tubulin controls the initiation of processive dynein-dynactin motility. *EMBO J.* **35**, 1175–1185 (2016). doi:10.15252/embj.201593071 Medline

38. P. Sartori, V. F. Geyer, J. Howard, F. Jülicher, Curvature regulation of the ciliary beat through axonemal twist. *Phys. Rev. E* **94**, 042426 (2016). doi:10.1103/PhysRevE.94.042426 Medline

39. C. B. Lindemann, K. A. Lesich, Functional anatomy of the mammalian sperm flagellum. *Cytoskeleton* **73**, 652–669 (2016). doi:10.1002/cm.21338 Medline

40. M. Fujimura, M. Okuno, Requirement of the fixed end for spontaneous beating in flagella. *J. Exp. Biol.* **209**, 1336–1343 (2006). doi:10.1242/jeb.02131 Medline

41. E. F. Smith, P. Yang, The radial spokes and central apparatus: Mechano-chemical transducers that regulate flagellar motility. *Cell Motil. Cytoskeleton* **57**, 8–17 (2004). doi:10.1002/cm.10155 Medline

42. T. Kubo, Y. Hou, D. A. Cochran, G. B. Witman, T. Oda, A microtubule-dynein tethering complex regulates the axonemal inner dynein *f* (I1). *Mol. Biol. Cell* **29**, 1060–1074 (2018). doi:10.1091/mbc.E17-11-0689 Medline

43. R. Orbach, J. Howard, The dynamic and structural properties of axonemal tubulins support the high length stability of cilia. *Nat. Commun.* **10**, 1838 (2019). doi:10.1038/s41467-019-09779-6 Medline

44. T. Ishikawa, Axoneme structure from motile cilia. *Cold Spring Harbor Perspect. Biol.* **9**, a028076 (2017). doi:10.1101/cshperspect.a028076 Medline

45. D. Wloga, D. M. Webster, K. Rogowski, M.-H. Bré, N. Levilliers, M. Jerka-Dziadosz, C. Janke, S. T. Dougan, J. Gaertig, TTLL3 Is a tubulin glycine ligase that regulates the assembly of cilia. *Dev. Cell* **16**, 867–876 (2009). doi:10.1016/j.devcel.2009.04.008 Medline

46. D. Wloga, D. Dave, J. Meagley, K. Rogowski, M. Jerka-Dziadosz, J. Gaertig, Hyperglutamylation of tubulin can either stabilize or destabilize microtubules in the same cell. *Eukaryot. Cell* **9**, 184–193 (2010). doi:10.1128/EC.00176-09 Medline

47. C. Janke, The tubulin code: Molecular components, readout mechanisms, and functions. *J. Cell Biol.* **206**, 461–472 (2014). doi:10.1083/jcb.201406055 Medline

48. T. Giordano, S. Gadadhar, S. Bodakuntla, J. Straub, S. Leboucher, G. Martinez, W. Chemlali, C. Bosc, A. Andrieux, I. Bieche, C. Arnoult, S. Geimer, C. Janke, Loss of the deglutamylase CCP5 perturbs multiple steps of spermatogenesis and leads to male infertility. *J. Cell Sci.* **132**, jcs226951 (2019). doi:10.1242/jcs.226951 Medline

49. Z.-E. Kherraf, M. Christou-Kent, T. Karaouzene, A. Amiri-Yekta, G. Martinez, A. S. Vargas, E. Lambert, C. Borel, B. Dorphin, I. Aknin-Seifer, M. J. Mitchell, C. Metzler-Guillemain, J. Escoffier, S. Nef, M. Grepillat, N. Thierry-Mieg, V. Satre, M. Bailly, F. Boitrelle, K. Pernet-Gallay, S. Hennebicq, J. Fauré, S. P. Bottari, C. Coutton, P. F. Ray, C. Arnoult, SPINK2 deficiency causes infertility by inducing sperm defects in heterozygotes and azoospermia in homozygotes. *EMBO Mol. Med.* **9**, 1132–1149 (2017). doi:10.15252/emmm.201607461 Medline

50. S. M. Curi, J. I. Ariagno, P. H. Chenlo, G. R. Mendeluk, M. N. Pugliese, L. M. Sardi Segovia, H. E. H. Repetto, A. M. Blanco, Asthenozoospermia: Analysis of a large population. *Arch. Androl.* **49**, 343–349 (2003). doi:10.1080/01485010390219656 Medline

51. T. R. Birkhead, D. J. Hosken, S. Pitnick, in *Sperm Biology: An Evolutionary Perspective*, T. R. Birkhead, D. J. Hosken, S. Pitnick, Eds. (Academic Press, 2009), pp. vii–viii.

52. L. Alvarez, The tailored sperm cell. *J. Plant Res.* **130**, 455–464 (2017). doi:10.1007/s10265-017-0936-2 Medline

53. Y. Lallemand, V. Luria, R. Haffner-Krausz, P. Lonai, Maternally expressed PGK-Cre transgene as a tool for early and uniform activation of the Cre site-specific recombinase. *Transgenic Res.* **7**, 105–112 (1998). doi:10.1023/A:1008868325009 Medline

54. N. Delgehyr, A. Meunier, M. Faucourt, M. Bosch Grau, L. Strehl, C. Janke, N. Spassky, Ependymal cell differentiation, from monociliated to multiciliated cells. *Methods Cell Biol.* **127**, 19–35 (2015). doi:10.1016/bs.mcb.2015.01.004 Medline

55. S. M. Q. Hussaini, H. Jun, C. H. Cho, H. J. Kim, W. R. Kim, M.-H. Jang, Heat-induced antigen retrieval: An effective method to detect and identify progenitor cell types during adult hippocampal neurogenesis. *J. Vis. Exp.* **78**, e50769 (2013). doi:10.3791/50769 Medline

56. M. M. Magiera, C. Janke, "Investigating tubulin posttranslational modifications with specific antibodies" in *Microtubules, In Vitro*, vol. 115 of *Methods in Cell Biology*, J. J. Correia, L. Wilson, Eds. (Academic Press, 2013), pp. 247–267.

57. A. J. Al Omran, H. C. Saternos, T. Liu, S. M. Nauli, W. A. AbouAlaiwi, Live imaging of the ependymal cilia in the lateral ventricles of the mouse brain. *J. Vis. Exp.* **100**, e52853 (2015). doi:10.3791/52853 Medline

58. C. M. Smith, J. Djakow, R. C. Free, P. Djakow, R. Lonnen, G. Williams, P. Pohunek, R. A. Hirst, A. J. Easton, P. W. Andrew, C. O'Callaghan, ciliaFA: A research tool for automated, high-throughput measurement of ciliary beat frequency using freely available software. *Cilia* **1**, 14 (2012). doi:10.1186/2046-2530-1-14 Medline

59. S.-H. Lee, D. G. Grier, Holographic microscopy of holographically trapped three-dimensional structures. *Opt. Express* **15**, 1505–1512 (2007). doi:10.1364/OE.15.001505 Medline

60. L. Wilson, R. Zhang 3rd, Localization of weak scatterers in digital holographic microscopy using Rayleigh-Sommerfeld back-propagation. *Opt. Express* **20**, 16735 (2012). doi:10.1364/OE.20.016735

61. L. Björndahl, I. Söderlund, U. Kvist, Evaluation of the one-step eosin-nigrosin staining technique for human sperm vitality assessment. *Hum. Reprod.* **18**, 813–816 (2003). doi:10.1093/humrep/deg199 Medline

62. X. Li, P. Mooney, S. Zheng, C. R. Booth, M. B. Braunfeld, S. Gubbens, D. A. Agard, Y. Cheng, Electron counting and beam-induced motion correction enable near-atomic-resolution single-particle cryo-EM. *Nat. Methods* **10**, 584–590 (2013). doi:10.1038/nmeth.2472 Medline

63. J. R. Kremer, D. N. Mastronarde, J. R. McIntosh, Computer visualization of three-dimensional image data using IMOD. *J. Struct. Biol.* **116**, 71–76 (1996). doi:10.1006/jsbi.1996.0013 Medline

64. Q. Xiong, M. K. Morphew, C. L. Schwartz, A. H. Hoenger, D. N. Mastronarde, CTF determination and correction for low dose tomographic tilt series. *J. Struct. Biol.* **168**, 378–387 (2009). doi:10.1016/j.jsb.2009.08.016 Medline

65. J. M. Heumann, A. Hoenger, D. N. Mastronarde, Clustering and variance maps for cryo-electron tomography using wedge-masked differences. *J. Struct. Biol.* **175**, 288–299 (2011). doi:10.1016/j.jsb.2011.05.011 Medline

66. E. F. Pettersen, T. D. Goddard, C. C. Huang, G. S. Couch, D. M. Greenblatt, E. C. Meng, T. E. Ferrin, UCSF Chimera—A visualization system for exploratory research and analysis. *J. Comput. Chem.* **25**, 1605–1612 (2004). doi:10.1002/jcc.20084 Medline